



B3AM: A beamforming toolbox for three-component ambient seismic noise analysis

Katrin L  er *¹, Claudia Finger ²

¹Department of Geoscience and Engineering, TU Delft, The Netherlands, ²Fraunhofer IEG, Fraunhofer Institution for Energy Infrastructures and Geothermal Systems, Bochum, Germany

Author contributions: *Conceptualization:* K. L  er. *Methodology:* K. L  er, C. Finger. *Software:* K. L  er, C. Finger. *Writing - original draft:* K. L  er. *Writing - Review & Editing:* C. Finger.

Abstract We introduce the code package *B3AM* for beamforming of three-component ambient noise array data, which is available for MATLABTM and Python. We explain the theory behind three-component beamforming and polarisation analysis in particular, provide an overview of the workflow, and discuss the output using a worked example based on the MATLABTM implementation. The strength of the presented code package is the analysis of multiple beam response maps from multiple time windows. Hence, it provides statistical information about the ambient noise wavefield recorded over a period of time, such as the ratio of surface to body waves, average dispersion velocities, or dominant propagation direction. It can be used to validate assumptions made about the ambient noise wavefield in a particular location, helping to interpret results from other techniques, such as the analysis of horizontal-to-vertical spectral ratios or ambient noise interferometry, and enabling more precise monitoring of specific wavefield components. While designed initially with seismic networks in mind, *B3AM* is applicable over a wide range of frequencies and array sizes and can thus be adapted also for laboratory settings or civil engineering applications.

Production Editor:
Carmine Galasso
Handling Editor:
Paula Koelemeijer
Copy & Layout Editor:
Aisling O’Kane

Signed reviewer(s):
Marine Denolle

Received:
March 28, 2024
Accepted:
September 26, 2024
Published:
November 15, 2024

1 Motivation

Over the last two decades, ambient seismic noise methods gained more and more attention as cheap and practical tools to image and monitor internal structures and processes of the subsurface and the built environment (e.g., Nicolson et al., 2012; Salvermoser et al., 2015; Kennedy et al., 2022). While two-station methods estimating the Green’s function between two receivers (or sources) from cross-correlations of ambient noise have dominated the scene under the name of seismic interferometry (e.g., Wapenaar and Fokkema, 2006; Curtis et al., 2006; Galetti and Curtis, 2012), array-based methods such as the spatial autocorrelation method (Aki, 1957) and frequency-wavenumber techniques (Lacoss et al., 1969; Esmersoy et al., 1985; Riahi et al., 2013), commonly known as beamforming, have also become increasingly popular: in a recent paper, Qin and Lu (2024) highlight the ability to directly measure azimuth dependent properties as well as to extract multimode dispersion curves as major advantages of array-based ambient noise methods. As Yamaya et al. (2021) point out, the array-based SPAC technique assists SI in retrieving robust velocity profiles in strongly heterogeneous media. Under the SESAME project (<https://sesame.geopsy.org>) pioneering studies were conducted, investigating site characterisation with array data of ambient vibrations (e.g., Wathelet et al., 2008). Finger and L  er (2024) and Obiri et al. (2023) use beamforming of three-component array data to analyse the wavefield

composition and provide improved depth estimates of subsurface velocity changes, relevant for subsurface resource exploration as well as seismic hazard assessment.

As a result of its increasing popularity, a number of public codes for ambient noise analysis with seismic arrays became available over the years. Most tools focus on interferometric methods, computing and analysing cross-correlations between individual station pairs, such as *MSNoise* for monitoring velocity changes (Lecocq et al., 2014) or *NoisePy* for monitoring applications as well as surface wave dispersion analysis (Jiang and Denolle, 2020). Ermert et al. (2020) developed *noisi* to study sources of ambient noise and help interpret the results of auto- and cross-correlations. Since beamforming techniques have long been used in earthquake seismology (Rost and Thomas, 2002), early codes such as *SAC* (*Seismic Analysis Code*, Goldstein et al., 2003) are tuned towards transient wave rather than continuous data analysis. Single component ambient noise array data can be processed using *ObsPy* (Beyreuther et al., 2010), for example, which offers a signal processing routine for frequency-wavenumber analysis following either standard beamforming or the high-resolution Capon method (Capon, 1969). Recently, Sollberger et al. (2023) introduced *TwistPy* for combined analysis of single-component array data and six-component single-station data. The MATLABTM toolbox *MISARA* for array techniques (Minio et al., 2023) is designed particularly for volcano monitoring and includes a high degree of automated tasks, which minimizes the interaction and

*Corresponding author: k.loer@tudelft.nl

effort required by the user, but also limits the range of applications. Also *MISARA* works on vertical component data only. Two algorithms that account for three-component array data are *WaveDec* by [Maranò et al. \(2012\)](#) and the comprehensive *Geopsy* framework by [Wathelet et al. \(2020\)](#), which includes an array processing module. Both were developed for surface wave analysis in the context of site characterisation and therefore only discriminate between vertical, Love and Rayleigh wave polarisation.

Acknowledging the current trends (and gaps) and recognising the benefits array-based ambient noise analysis brings to the seismic community, this work outlines the theory and practical application of beamforming with a particular focus on the analysis of three-component ambient noise array data. Exploiting the full three-component particle motion information on multiple stations in an array allows us to distinguish between wave types and thus provides more accurate dispersion curves and the opportunity for additional analyses, for example, for wavefield composition or anisotropy. This paper gives a comprehensive summary of the functionality and output of the *B3AM* toolbox and explains in detail how the dominant wave type in a time window and its propagation properties are retrieved by analysing phase shifts across stations as well as across components. We describe the relationship between polarisation parameters, such as ellipticity or dip angle, and the corresponding phase shifts in the three-component data, linking an intuitive, human-readable representation to the mathematical implementation in the beamforming code. Our goal is to make the technique transparent and accessible thereby providing an opportunity for future improvements and adaptations for different scenarios by a diverse research community.

2 Theory

The three-component beamforming approach presented and applied in this work discriminates wave types in the ambient seismic noise wavefield based on three-component particle motion estimates. We explain in detail how this is implemented in *B3AM* and provide explicit examples for different wave types (body and surface waves). This chapter starts with a short review of single-component beamforming that highlights the computational cost of different implementations of the beamformer before elaborating on the three-component approach. We comment on the impact of the array design and explain how robust wavenumber and frequency limits can be estimated in practice.

2.1 Single-component beamforming

In both single- (vertical) and three-component beamforming, dominant velocity and direction of arrival of a wavefield are estimated based on the phase shifts observed between the different stations of the array. Phase shifts in the data are contained in the cross-spectral density matrix (CSDM)

$$S_{ij}(\omega) = s_i(\omega) \cdot s_j(\omega)^*, \quad (1)$$

where $s_i(\omega)$ and $s_j(\omega)$ are the Fourier transformed seismic data at frequency ω recorded at receivers $i \leq M$ and $j \leq M$, respectively, and $*$ denotes complex conjugation. Hence, the CSDM provides the cross-correlation between all receiver pairs in the frequency domain. Theoretical phase shifts for all M receiver locations \mathbf{r} caused by a wave with a particular wavenumber vector \mathbf{k} are computed in the array response vector ([Riahi et al., 2013](#); [Löer et al., 2018](#))

$$\mathbf{a}(\mathbf{k}) = \frac{1}{M} \exp(i\mathbf{k}\mathbf{r}). \quad (2)$$

Theoretical phase shifts between receiver pairs are computed in what we will call the array response matrix (ARM)

$$\mathbf{A}(\mathbf{k}) = \mathbf{a}(\mathbf{k}) \cdot \mathbf{a}(\mathbf{k})^*. \quad (3)$$

We can think of this matrix as the equivalent of the cross-spectral density matrix of the data for theoretical wave vectors \mathbf{k} . Comparison of the two via cross-correlation will identify the wave vector that results in the best match, i.e., gives the largest beam response

$$B(\omega, \mathbf{k}) = \mathbf{S}(\omega) \cdot \mathbf{A}(\mathbf{k})^*, \quad (4)$$

where $B(\omega, \mathbf{k})$ is real-valued and a function of the frequency ω and the wave vector \mathbf{k} . Equation 4 is equivalent to the standard beamforming procedure ([Riahi et al., 2013](#); [Löer et al., 2018](#))

$$B(\omega, \mathbf{k}) = \mathbf{a}(\mathbf{k}) \cdot \mathbf{S}(\omega) \cdot \mathbf{a}(\mathbf{k})^*. \quad (5)$$

In practice, the implementation of Equation 4 requires looping over \mathbf{k} and thus is computationally very expensive. The modified version in Equation 5 is slightly faster and still allows us to modify the CSDM, as is done in more advanced beamforming techniques such as MUSIC ([Schmidt, 1986](#)) or Capon beamforming ([Capon, 1969](#)). In cases, however, where the CSDM does not need to be computed, beamforming can be implemented in the most cost-effective way using

$$B(\omega, \mathbf{k}) = |\mathbf{s} \cdot \mathbf{a}(\mathbf{k})^*|^2 \quad (6)$$

([Löer et al., 2018](#)) instead. In the accompanying code, the user can choose between these two different forms of implementation (Equation 5 or 6).

2.2 Three-component beamforming

In single-component beamforming, we consider the phase shifts recorded on different *stations*, and how these are related to the velocity and direction of arrival of the dominant wave. When three-component data is available, we can also consider the phase shifts across the three *components* that contain useful information about the polarisation and hence the type of wave that is recorded. If a seismic station records ground movement in three directions – East (E), North (N), and vertical (Z) – we can observe a phase shift between the vertical and horizontal components as a result of the wave's particle motion. The particle motion of a P-wave, for example, is parallel to the wave's propagation direction, whereas for an S-wave, the particle motion is perpendicular to the propagation direction, with SV and SH waves

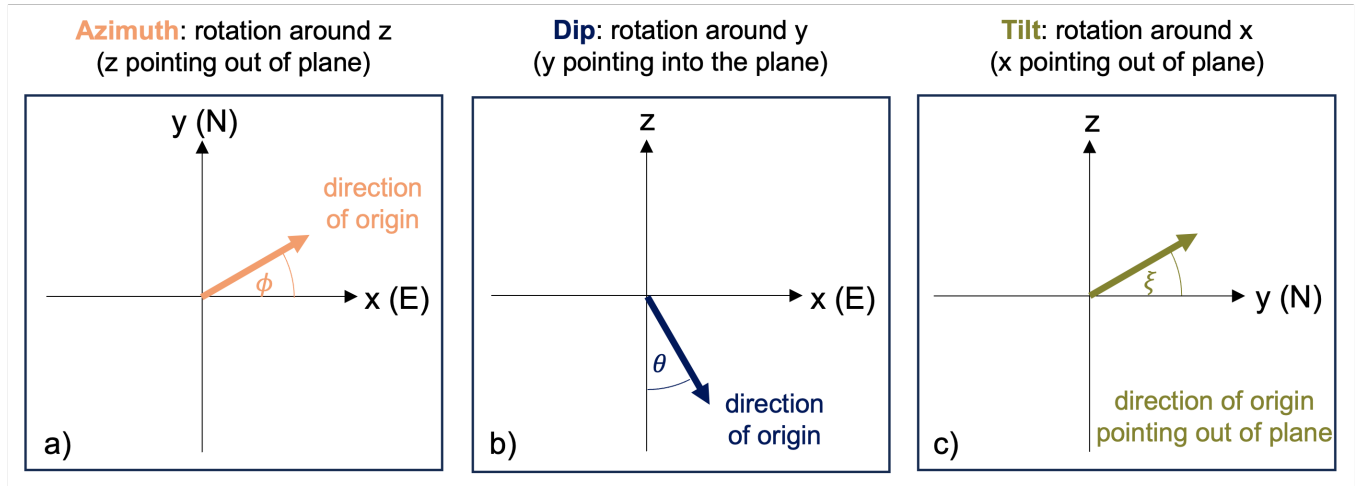


Figure 1 Coordinate systems and angle rotation conventions used in Equations 7 to 10. a) The azimuth refers to the propagation direction of the wave on the surface plane, b) the dip refers to the incidence angle at the surface ($\theta = 90^\circ$ for surface waves), and c) the tilt describes out-of-plane propagation, discriminating SV and SH as well as prograde and retrograde Rayleigh waves.

oscillating again perpendicular to each other. Rayleigh waves have an elliptical particle motion confined to the vertical direction and the propagation direction, while Love waves behave like SH waves in terms of particle motion. Azimuth and incidence angle also influence the phase shifts across the three components. Example figures for each wave type are provided in the Supplementary Material. The polarisation phase shifts can be derived from a set of three rotation matrices:

$$\mathbf{R}_x = \begin{bmatrix} 1 & 0 & 0 \\ 0 & \cos(\xi) & -\sin(\xi) \\ 0 & \sin(\xi) & \cos(\xi) \end{bmatrix} \quad (7)$$

$$\mathbf{R}_y = \begin{bmatrix} -\sin(\theta) & 0 & \cos(\theta) \\ 0 & 1 & 0 \\ \cos(\theta) & 0 & \sin(\theta) \end{bmatrix} \quad (8)$$

$$\mathbf{R}_z = \begin{bmatrix} \cos(\phi) & -\sin(\phi) & 0 \\ \sin(\phi) & \cos(\phi) & 0 \\ 0 & 0 & 1 \end{bmatrix} \quad (9)$$

Here, R_x describes a rotation around the x-axis (counter-clockwise from North when looking towards East), R_y describes rotation around the y-axis (counter-clockwise from vertical when looking towards North), and R_z describes rotation around z-axis (counter-clockwise from East when looking down). Figure 1 visualises the coordinate systems used for the angles ϕ , θ , and ξ , respectively. It follows that R_z accounts for the phase shift introduced by the azimuth ϕ (direction of arrival on the surface) and R_y relates to the incidence angle or dip from vertical (θ), that is, for surface waves $\theta = 90^\circ$. R_x accounts for the phase shift incurred by the tilt ξ , which describes particle motion in relation to the plane of propagation (x-z plane) and is used to discriminate between SV and SH waves as well as pro- and retrograde Rayleigh waves (see Table 1).

While the azimuth affects the particle motion and thus the phase shifts on the two horizontal components,

it is not a parameter that helps to distinguish different wave types. Disregarding the azimuth rotation (\mathbf{R}_z), or assuming $\phi = 0^\circ$, we can write \mathbf{R}_y and \mathbf{R}_x as a single rotation matrix that is a function of dip θ and tilt ξ :

$$\begin{aligned} \mathbf{R}(\phi = 0^\circ, \theta, \xi) &= \mathbf{R}_y \cdot \mathbf{R}_x \\ &= \begin{bmatrix} -\sin(\theta) & \cos(\theta) \sin(\xi) & \cos(\theta) \cos(\xi) \\ 0 & \cos(\xi) & -\sin(\xi) \\ \cos(\theta) & \sin(\theta) \sin(\xi) & \sin(\theta) \cos(\xi) \end{bmatrix} \end{aligned} \quad (10)$$

Another important parameter to describe Rayleigh waves, but also used here to constrain the particle motion of all other wave types, is the ellipticity e . We define the value of e between 0 and 2, where 0 is purely horizontal motion, 1 is circular motion, and 2 is purely vertical motion. Using the rotation matrix \mathbf{R} (see Equation 10), the beamformer transforms dip θ , tilt ξ , and ellipticity e into a complex valued, three-component phase shift $\mathbf{z}(\theta, \xi, e)$ according to:

$$\mathbf{z}(\theta, \xi, e) = \mathbf{R}\mathbf{h}_1 - i\mathbf{R}\mathbf{h}_2, \quad (11)$$

where vectors \mathbf{h}_1 and \mathbf{h}_2 represent the horizontal and vertical half axis of the particle motion ellipse, respectively, as in Figure 2, and are defined for

$$e \leq 1 \text{ as } \mathbf{h}_1 = [1; 0; 0] \text{ and } \mathbf{h}_2 = [0; 0; e] \quad (12a)$$

$$e \geq 1 \text{ as } \mathbf{h}_1 = [2 - e; 0; 0] \text{ and } \mathbf{h}_2 = [0; 0; 1]. \quad (12b)$$

Table 1 demonstrates that the resulting phase shifts are unique for each wave type, dip, and ellipticity. Comparing our definition of ellipticity to the energy ratio between horizontal and vertical components (H/V), a common measure for Rayleigh wave particle motion, we find that:

$$\text{if } e \leq 1 \text{ then } \frac{H}{V} = \frac{1}{e} \quad (13a)$$

$$\text{if } e \geq 1 \text{ then } \frac{H}{V} = 2 - e. \quad (13b)$$

	P-wave	SH/Love wave	SV-wave	Retrogr. Rayleigh wave		Progr. Rayleigh wave	
wave id.	0	1	2	3		4	
polarisation id.	1-10	11	12-21	22-40		41-59	
dip (θ)	0° : 10° : 90°	90°	0° : 10° : 90°	90°		90°	
ellipticity (e)	0	2	2	0.1 : 0.1 : 1.9		0.1 : 0.1 : 1.9	
tilt (ξ)	180°	90°	180°	0°		180°	
				$e < 1$	$e > 1$	$e < 1$	$e > 1$
X phase shift	$-\sin(\theta)$	0	$i \cos(\theta)$	-1	$-(2-e)$	-1	$-(2-e)$
Y phase shift	0	i	0	0	0	0	0
Z phase shift	$\cos \theta$	0	$i \sin \theta$	$-ie$	$-i$	ie	i

Table 1 Polarisation parameters (top) and corresponding phase shifts (bottom) for the five different wave types. Phase shifts correspond to the vector $\mathbf{z} = \mathbf{R}\mathbf{a} - i\mathbf{R}\mathbf{b}$ (Equation 11) and are computed for an azimuth (direction of origin) of $\phi = 0^\circ$; i is the imaginary unit. Wave id. refers to an index given to each identified wave type in the beamforming process. Polarisation id. is the index specific to each polarisation state.

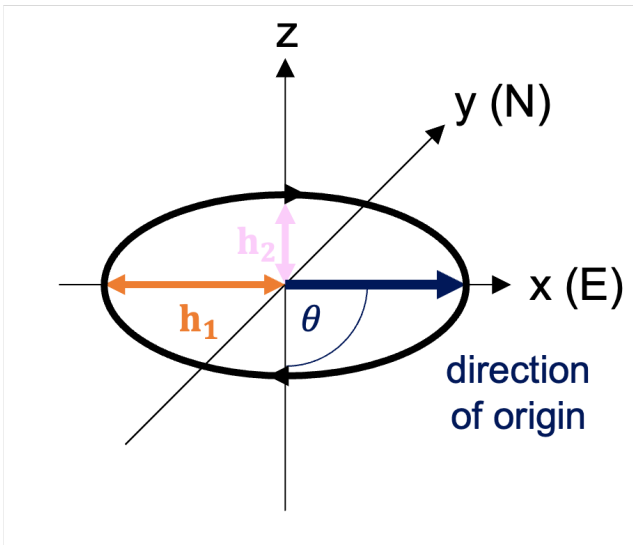


Figure 2 Particle motion ellipse of a retrograde Rayleigh wave with ellipticity $e < 1$. h_1 and h_2 represent the horizontal and vertical half axis, respectively, as shown in Equation 13a.

Figure 2 shows an example of the elliptical particle motion of a retrograde Rayleigh wave with ellipticity $e < 1$.

In the 3C beamformer, the wavenumber information from phase shifts across stations is combined with the polarisation information obtained from phase shifts across components: for each time window, the beamformer performs a three-dimensional grid search over the wavenumber vector \mathbf{k} , comprising horizontal wavenumber k and azimuth ϕ , and a predefined range of polarisation states $p = p(\theta, e, \xi)$ (see Table 1) to find the best match with the data, based on

$$B^{3C}(\mathbf{k}, p) = \mathbf{w}(\mathbf{k}, p) \cdot \mathbf{S}^{3C} \cdot \mathbf{w}(\mathbf{k}, p)^* \quad (14)$$

(Löer et al., 2018), where $\mathbf{w}(\mathbf{k}, p) = \mathbf{z}(p) \otimes \mathbf{a}(\mathbf{k})$ are the total phase shifts comprising phase shifts across stations $\mathbf{a}(\mathbf{k})$ (see Equation 2) and phase shifts across components $\mathbf{z}(p)$ (see Equation 11). \mathbf{S}^{3C} is the $3M \times 3M$ CSDM of the three-component data, where M is the number of stations. Finally, for each wavenumber-

azimuth pair, only the beam response at the polarisation state that yields the maximum response is stored. This reduces the 3D grid to a 2D beam response matrix (Figure 3a) plus a polarisation matrix (Figure 3b) that contains the dominant polarisation state at each wavenumber-azimuth pair (cf. Riahi et al., 2013). An alternative approach retaining all polarisation states has been developed by Wagner (1996) and applied, for example, by Gal et al. (2016) and Liu et al. (2016).

2.3 Array design considerations

The size of the array, that is, the minimum and maximum station spacing but also the relative locations of the stations, determine the resolvable wavenumber range. A commonly applied rule of thumb after Tokimatsu (1997) defines resolvable wavelengths λ as a function of minimum and maximum station spacing, d_{min} and d_{max} , respectively:

$$2d_{min} < \lambda < 3d_{max}. \quad (15)$$

This approach does not consider, however, that the spacing is not necessarily the same in all directions, and hence resolution can vary with azimuth. More recent studies (Wathelet et al., 2008) tested the relationship with regards to the accuracy of dispersion curves and found that more conservative assumptions lead to more robust results. They suggest to determine the wavenumber limits based on the theoretical array response function that account for the actual geometry of the array. The B3AM toolbox computes initial wavenumber limits based on Tokimatsu's rule of thumb (Equation 15; Tokimatsu, 1997) and lets the user check their appropriateness by providing the array response functions with wavenumber limits indicated (Figure 7). The user can then refine the choice of minimum and maximum wavenumber before running the beamformer.

The resolvable frequency range depends on the wavenumber range and the local velocities ($f = kv$). The best way to calculate it would therefore use (theoretical) local dispersion curves that provide velocity or wavenumber as a function of frequency. As this information is often exactly what should be obtained from the ambient noise analysis, and thus not available a priori, we suggest following the reversed approach: the

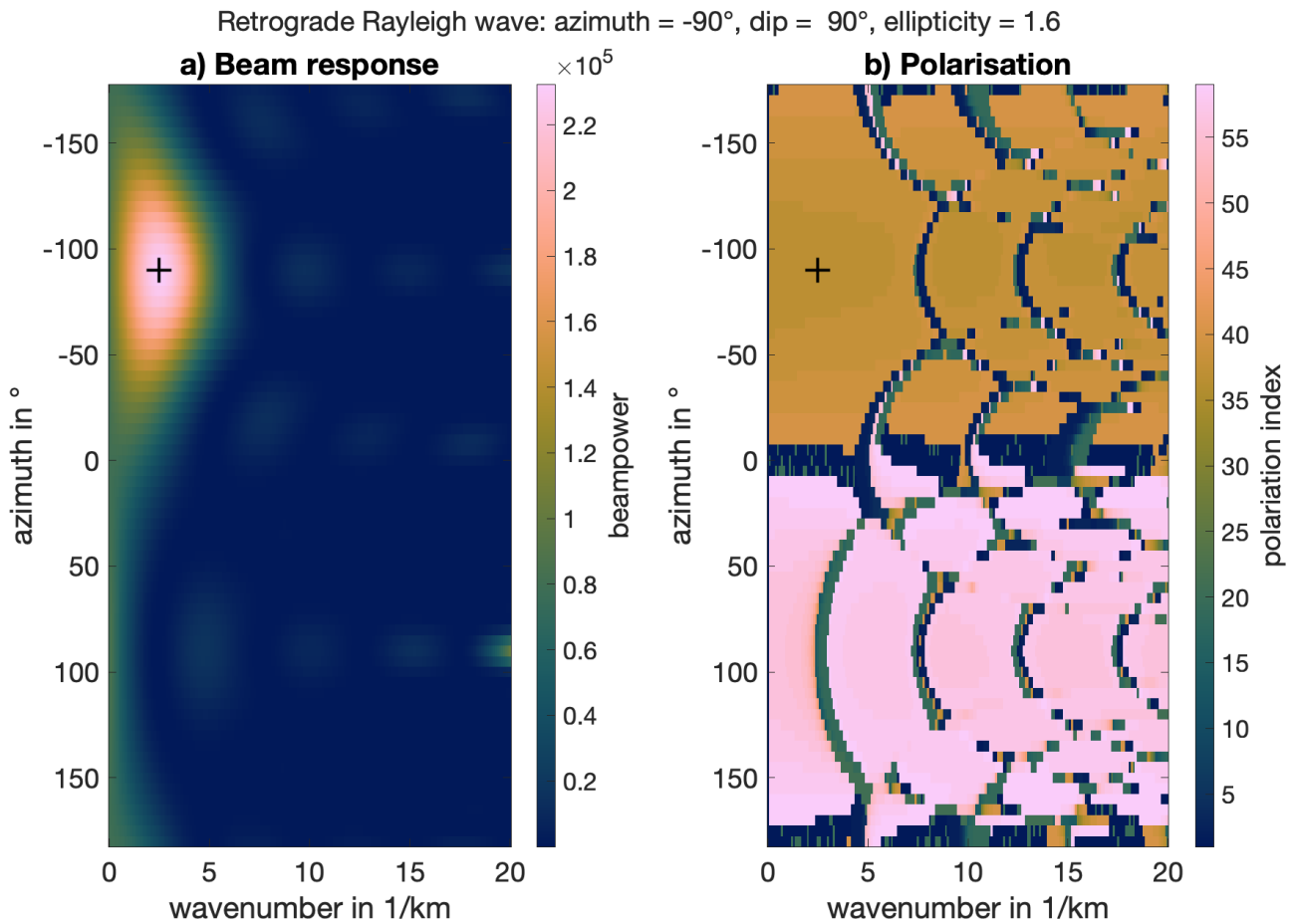


Figure 3 Beam response (a) and polarisation map (b) as a function of azimuth and wavenumber for a single time window. The black cross marks the maximum beam response in (a) and the corresponding polarisation in (b). The colour bar identifies different polarisation states according to Table 1. The plot was created with the script `plot_PandQ.m`. Synthetic data were modelled with a finite-difference wave propagation code from a single source in a homogeneous half-space with a free surface. The chosen time window captures the Rayleigh wave arrival at the array.

user defines a desired or practical frequency range, for example, based on assumptions about the dominant frequencies of prevalent noise sources, and the resulting velocity limits are then calculated based on wavenumber and frequency values. These limits are displayed in the resulting dispersion curve plot, indicating confidence bounds of the results (Figure 10).

Alternatively, the wavelength limits can be estimated using Equation 15. Assuming a depth sensitivity in the order of a quarter of the wavelength limits and using rough estimates of the expected velocity range in that depth, a preliminary frequency range can be estimated.

3 Program description

In this section, we first provide a general overview of the content and workflow of the *B3AM* package before outlining its handling in detail using an example data set alongside instructions to reproduce the results shown in this paper. The *B3AM* package for MATLAB™ can be downloaded from GitHub® (<https://github.com/katrinloer/B3AM>) or MATLAB™ FileExchange (<https://nl.mathworks.com/matlabcentral/fileexchange/128489-b3am>), a very

similar version for Python and accompanying documentation are also available from GitHub® (<https://github.com/cl-finger/B3Ampy>). Note that the following description focuses on the implementation in MATLAB™.

3.1 Requirements and content of the package

The package comprises the MATLAB™ scripts to prepare the data, perform the beamforming process, and visualise its outcome. The main scripts as highlighted in Figure 4 can be found in the main directory. The subfolder *b3am* contains auxiliary scripts and functions used during data processing and beamforming. The subfolder *plot* contains auxiliary scripts used for plotting. Note that these scripts make use of Cramer’s colour scheme for scientific plotting (Cramer, 2018), which need to be downloaded separately (e.g., <https://doi.org/10.5281/zenodo.1243862>). Example figures can be found in *Figures* while *IN* and *OUT* are the default input and output folders, respectively.

Seismic data needs to be converted into MATLAB™ structures (.mat files), that is, one file per day that contains time series data from all stations and all channels,

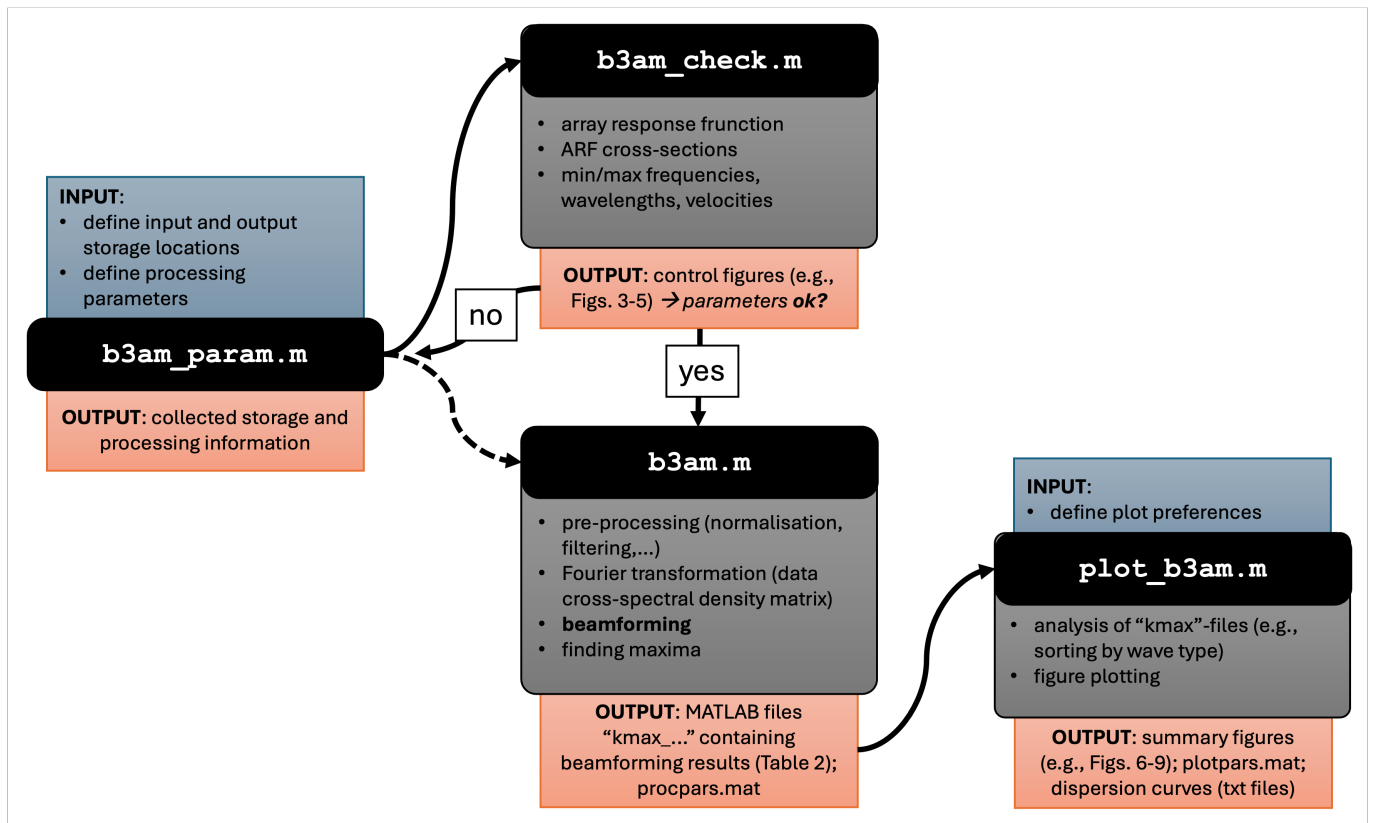


Figure 4 Outline of the workflow and use of scripts provided with the *B3AM* package. Blue boxes indicate a required user interaction, red boxes indicate the output of a piece of code, and grey boxes outline the main tasks of the respective code. All parameters are set in `b3am_param.m` and checked in `b3am_check.m` before the main script `b3am.m` is executed. A subset of the results can be plotted with `plot_b3am.m`.

sorted by channel in the order (1) East, (2) North, and (3) vertical. Data downloaded from the Seismological Facility for the Advancement of Geoscience (SAGE, before IRIS) directly into MATLAB™ needs to be converted using the script `b3am_convert_iris.m` to adapt the ordering of channels. Data in SEGY or SEED format can be converted using the scripts `b3am_convert_seggy.m` or `b3am_convert_seed.m`, respectively. The required input for these scripts is specified in the code. The name of the new file is `DAT_NN_yyyyddd.mat`, where `NN` are two letters representing the network (the Parkfield network has the code `XN`, for example), `yyyy` denotes the year (e.g., 2022) and `ddd` gives the day of the year (between 1 and 365). This information is retrieved automatically from the original data file. The new data file will be created in the folder `IN` unless specified otherwise.

3.2 Workflow and output

Figure 4 outlines the workflow and use of the main beamforming scripts. The core script of the package is `b3am.m`, accompanied by the script `b3am_param.m`, in which the user specifies the processing and beamforming parameters. After `b3am_param.m` has been configured, `b3am.m` can be executed without any further intervention. It is recommended though to use `b3am_check.m` to test if the specified parameters result in suitable wavenumber and velocity ranges, and adjusting those, before starting the beamformer.

In `b3am.m`, four major steps are performed succes-

sively:

1. data pre-processing (can include resampling, spectral and/or temporal normalisation, filtering),
2. Fourier transformation,
3. frequency-wavenumber analysis (beamforming),
4. identification of maxima in the beam response maps.

The Fourier transformed data are stored temporarily in the folder `tmpFT/` as one file per frequency named after the frequency (e.g., `0.200.mat`). Each `.mat` file contains a MATLAB™ structure `DFT` with fields `DFT.data` (containing the spectral amplitudes), `DFT.h` (containing header information such as station coordinates), and `DFT.procpars` (containing processing parameters, such as computing mode or wavenumber grid). Note that the files in folder `tmpFT` will be over-written each time a new file is processed. The size of `DFT.data` corresponds to the number of time windows times the total number of channels (number of stations times three).

The final output from `b3am.m` are the properties of all maxima picked in the beam response matrix (cf. Equation 14). By default, the detected maxima and their properties are saved in `OUT/kmax` as one `.mat`-file per day and frequency called `kmax_NN_yyyyddd_ffff.mat`, where `ffff` is the frequency (for other naming conventions see section 3.1).

Variable	Format	Content	Values
a_all	[nwin × nmax]	beam response amplitude	
kr_all	[nwin × nmax]	beam response wavenumber in 1/m	between 0 and kmax
kth_all	[nwin × nmax]	beam response azimuth in rad	between $-\pi$ and π
pola_all	[nwin × nmax × 4]	polarisation parameters	ϕ, θ, e, ξ
pola_ind	[nwin × nmax]	polarisation index	varies with e and θ (default 1 – 59)
wave_ind	[nwin × nmax]	wave type index	0, 1, 2, 3, 4

Table 2 Output variables stored in kmax-files characterising the maxima picked in the beam response maps. nwin denotes the number of time windows and nmax the maximum number of maxima detected in a single time window. See Table 1 for further details.

Each file contains six variables that are explained in Table 2. Note that beam response and polarisation matrices are currently not stored as the code is designed for large datasets where beam responses of 100s of time windows are considered individually and the storage requirements for these would be excessive. After executing `b3am.m` these matrices will be in the workspace for the last frequency that was processed and can be plotted using the script `plot_PandQ.m`.

An overview of the results can be plotted using `plot_b3am.m`. Note that the provided figures are by no means exhaustive and that the information contained in the output files can be displayed in various other ways to highlight and analyse further properties of the wavefield, such as ellipticity or anisotropy. After executing `plot_b3am.m`, dispersion curves for Love and Rayleigh waves will be saved to the chosen output folder (`OUT/kmax` by default) as txt-files.

In the following, we explain the implementation and output of B3AM based on an example data set. To familiarise with the B3AM package we encourage the reader to try to reproduce the figures in this paper by following the instructions below.

3.3 Example

To start working with B3AM, all files and folders from the GitHub® repository must be downloaded into one directory. Alternatively, the toolbox file `B3AM.mltbx`, a MATLAB™ add-on, can be downloaded and installed. The example is based on one day of ambient noise data recorded at the Parkfield array in California, US (Figure 5; Thurber and Roecker, 2000). The data are publicly available from the Seismological Facility for the Advancement of Geoscience (SAGE, former IRIS), and can be downloaded directly into MATLAB™. For comparison, the beamformer output data and figures for this example are provided in the folder `Example_Parkfield`.

3.3.1 Data download from SAGE

To load seismic data into MATLAB™, the script `irisFetch.m` (<http://ds.iris.edu/ds/nodes/dmc/software/downloads/irisfetch.m/>) and the Java library (<http://ds.iris.edu/ds/nodes/dmc/software/downloads/IRIS-WS/2-20-1/#Download>) are required. The script `iris_getrawdata_example.m` provided with the B3AM package can be used to download data from the Parkfield (or another) array. In the script, the

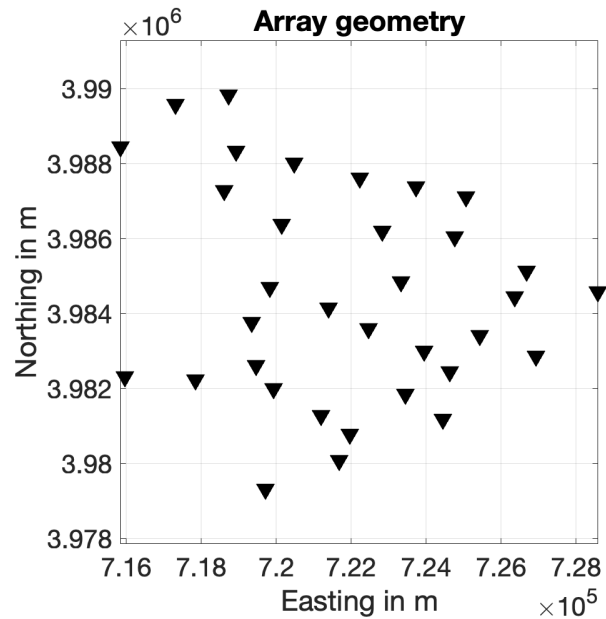


Figure 5 Station layout of the Parkfield array on 2 December 2002 as plotted by `b3am_check.m`.

path to the `irisFetch.m` script and the Java library need to be specified as both will be used in `iris_getrawdata_example.m`. Further parameters to be defined are the start and end date, the network code, names of stations in the network, channels, and storage location. Examples for these clarifying the required format are provided in the script. Expect the download to take up to a few minutes per station for a single day of data depending on network speed (here, it took around 25 minutes to download data from 34 stations).

3.3.2 Rearranging the data for 3C beamforming

The data download results in one MATLAB™-file per day (`RAW_NN_yyyyddd.mat`, see section 3.1 for naming conventions) containing data for all stations and all components. These need to be re-sorted for the beamformer such that East components of all stations come first, then North, then Vertical. This is done in the script `b3am_convert_iris.m`. The script requires the path to the folder `b3am` that contains auxiliary functions, in- and output directories for the data, and the file(s) that need to be converted. Running the script yields one new file

per day (DAT_NN_yyyyddd.mat). Rearranging the data should only take a few seconds per station per day.

Note that the length of the data is checked and compared to a minimum value (default is $24\text{h} = 86\,400\text{s}$). Traces that are too short can either be deleted (`traceflag = 'delete'`) or appended with zeros (`traceflag = 'append'`, default). The file `info_iris2dat_NN_yyyyddd.txt` in the defined output directory contains information about each trace. Reducing the minimum length will keep more stations, as a single missing sample will lead to the rejection of the full trace (for all three components) if `'delete'` is chosen. `b3am_convert_iris.m` also creates the file `stations_utm_NN_yyyyddd.txt` containing all station names with their latitude and longitude converted to x and y UTM-coordinates.

3.3.3 Set beamforming parameters

After rearranging the data, we prepare the beamformer. Open the script `b3am_param.m` and adjust the processing and beamforming parameters for the Parkfield data according to Listing 1.

Default values are to be used for azimuth (5°), dip (10°), ellipticity (`e=0.1:0.1:1.9`), window length (`twinf=10`), where `twinf` denotes a multiple of the largest period in the data (the next power of two is used in terms of samples to speed up the fast Fourier transformation), and number of workers (only relevant

if `para=1`). These variables can be commented in the code.

Running `b3am_check.m` returns a plot of the array geometry (Figure 5), the array response function (ARF, Figure 6 and 7), and the velocity resolution. Colourmaps after Cramer (2018) need to be installed if the same colour scheme is to be used (the corresponding path must be provided at the beginning of the script). Setting `save_figs = true` will store the figures in PNG format in the folder `Figures`.

The ARF cross-sections (Figure 7) help to assess whether the minimum and maximum wavenumbers have been set correctly. `kmax` corresponds with the upper limit of the x-axis, `kmin` is provided by the thick black vertical line. All wavenumber values (grey curves) to the right of this line should be below the half height of the peak amplitude (dotted horizontal line; cf. Wathelet et al., 2008). The output in the MATLAB™ Command Window provides further information on array statistics, wavenumber resolution, and minimum resolvable velocity.

3.3.4 Run the beamformer

Executing the main script `b3am.m` will perform data processing (filtering, normalisation), Fourier transformation, and beamforming. The Command Window documents its progress. Once the beamforming is finished successfully, the output will be stored

Listing 1 Processing parameters for Parkfield example to be defined in `b3am_param.m`.

```
%% Pre-processing
%-----
resampled_data = 0;      % Downsample to new sampling rate? 0 or 1
    snew = 25;
specwhite = 0;          % Spectral whitening? 0 or 1
onebit = 1;             % One-bit normalization? 0 or 1
trunc3std = 0;         % Truncate at 3x the standard deviation (Roux et al., 2005)? 0 or 1
ramnorm = 0;           % Running-absolute-mean normalization (Bensen et al., 2007)? 0 or 1
bpfiler = 1;           % Band-pass filter? 0 or 1
    N = 4;              % order of filter
    W = [0.1 1.0];      % cut-off frequencies in Hz

%% Fourier Transformation
%-----
% Provide frequency range of interest and step size in Hz:
fmin = 0.1;
fmax = 0.5;
fstep = 0.02;

%% FK computation
%-----
% Wavenumber resolution (grid over which to compute the FK spectra [1/km])
kres = 201;            % number of values between kmin and kmax (default is 201)
kmax = 1 / 1000;       % maximum wavenumber in 1/m (default computed from station spacing)
kmin = 0.05 / 1000;    % minimum wavenumber in 1/m (default computed from station spacing)
% Find strongest peaks
% 0 < min_beam <= 1 (extrema must be larger than min_beam * maximum amplitude)
min_beam = 0.7;
% Compute spectral density matrix (SDM) or fast option
procpars.cmode = 'fast'; % SDM or fast
% Beamforming method:
% 'DS': conventional delay-and-sum beamforming
procpars.method = 'DS';
% Parallel computing?
para = 0; % 1 (yes) or 0 (no)
```

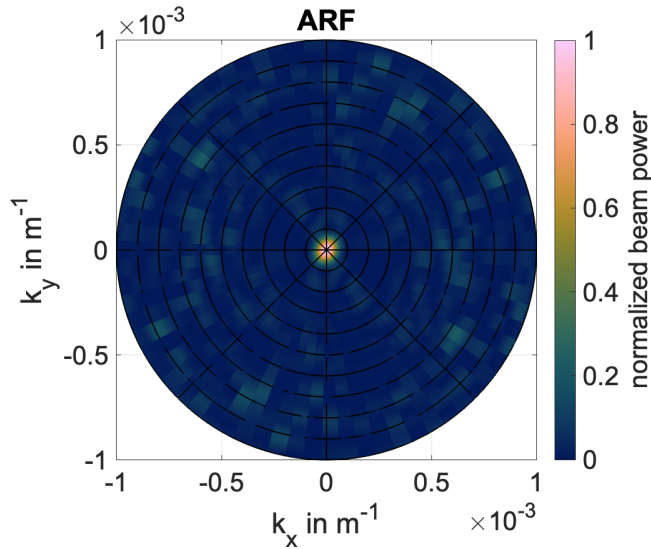



Figure 6 Normalized array response function (ARF) of the Parkfield array (Figure 5).

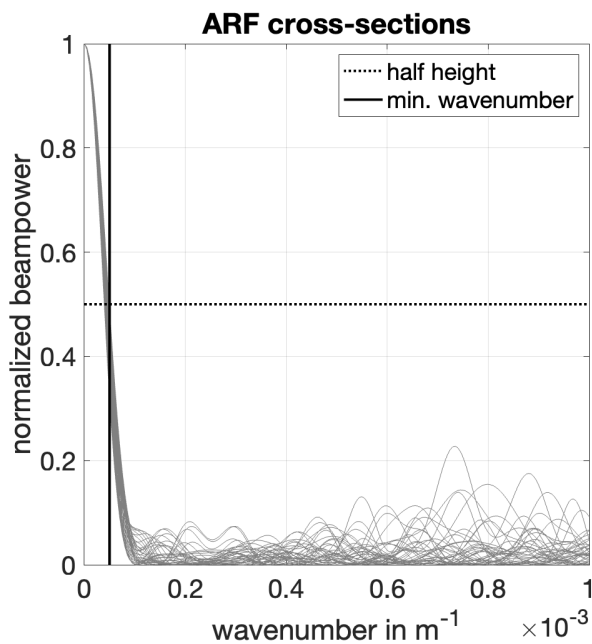


Figure 7 Normalized cross sections (gray) of the array response function (ARF; Figure 6) of the Parkfield array (Figure 5). The dotted horizontal line indicates the half height of the central peak and the black vertical line the chosen minimum wavenumber. The maximum wavenumber corresponds to the maximum of the x-axis

in the output directory defined in `b3am_param.m` as one MATLAB™-file per day and frequency, for example `kmax_XN_2001336_f0.100.mat` for a frequency of 0.1 Hz. There, also a copy of the processing parameters is stored as one file called `procpars.mat` and a copy of `b3am_param.m` including a time stamp (see example provided). Sequential processing of the example data set with the given parameters takes just over 1 min per frequency (25 min in total) on a Mac-

Book Pro, Apple M2 Pro. If access to multiple workers either on the computer or a cluster is available, the process can be accelerated by setting `para = 1` to enable parallel computing on all frequencies (under 15 min on 9 workers of the specified computer). Computing time depends non-linearly on the number of stations used and scales linearly with recording time, time window length, and number of frequencies. The choice of temporal normalisation will only affect the pre-processing time and increases significantly (around 7 min) for running-absolute-mean normalisation.

3.3.5 Plot the results

The script `plot_b3am.m` can be used to plot a summary of the results. By default, all figures produced in this script are stored in the folder `Figures`. In the script, under "Choose plot options", all variables should be set to true. Further options to be specified are `savefigs = true`, `maxflag = 'MAX1'`, `SNR = 1`, and `countflag = 'amp'`, which are explained below. For each time window that is processed, one beam response map is computed (Figure 3) that shows, which combination of frequency, wavenumber, and wave type matches the data in that time window best (because we compute these maps for several 1000s of time windows, they are not plotted or shown here). It is possible that different combinations of these three parameters provide a similar match, hence, the beam response map can have multiple peaks. Before plotting the results, we need to decide how many beam response peaks we want to consider in the analysis. This is done by setting the parameter `maxflag`. If `maxflag = 'MAX1'`, only the largest maximum in each beam response is considered. For `maxflag = 'NOMAX'` the number of maxima is not restricted. Sometimes the latter option can help to complete a dispersion curve when only a limited amount of data is available. However, it can also lead to ambiguities and misidentification of modes. Note that a threshold for the minimum amplitude of any peak is defined at the beginning, i.e., `min_beam` in `b3am_param.m`. The default value is 70 % of the maximum amplitude in the respective time window. Additionally, a noise threshold is applied automatically making sure that each detected maximum has an amplitude that is larger than the mean plus three times the standard deviation (this is implemented in the function `f_extrema24.m`). The role of `countflag` is important for wavefield composition plots and explained in the next chapter.

When figures are saved (`savefigs = true`), the plot settings will also be saved as `plotpars.mat` in the `Figures`-folder. The figures produced are

5. bar plot of wavefield composition (relative contributions; Figure 8),
6. bar plot of wavefield composition (absolute contributions),
7. line plot of wavefield composition (absolute contributions),
8. histogram of retrograde Rayleigh waves (wavenumber vs. frequency; Figure 9),

9. histogram of prograde Rayleigh waves (wavenumber vs. frequency),
10. histogram of Love waves (wavenumber vs. frequency),
11. dispersion curves for all three surface wave types (velocity vs. frequency; Figure 10), and
12. polar plots displaying direction of arrival for all 5 wave types (azimuth vs. frequency; Figure 11).

In the next chapter, these figures and their interpretation are explained in detail.

3.4 Output explained

3.4.1 Wavefield composition

The information displayed in the wavefield composition plots shows the number of detections by different wave types at different frequencies. If the option `countflag = 'amp'` is chosen, the amplitude of the beam response at each detection is considered. When `countflag = 'noamp'`, amplitudes are not considered and only number of detections is displayed. Note that this can change the relative contributions of different wave types, as there might be a lot of body waves detected at a certain frequency, however, with very low amplitudes. Their share under the 'noamp' option will thus be larger than for 'amp'.

3.4.2 Frequency-wavenumber histograms

Three figures are produced showing the histograms for retrograde Rayleigh, prograde Rayleigh, and Love waves. They display the wavenumber against frequency for the given wave type. The bin size is defined by the wavenumber grid and the frequency bins. Each detected wave is sorted into a bin according to its

wavenumber and frequency. The value for each bin is derived from the number of detections that fall into the bin and their respective beam response amplitudes. Hence, it displays not only occurrence but also the beam response value of a certain wave at a given frequency and wavenumber. When `histonorm = 'true'`, the histograms are normalised per frequency, i.e., the maximum in each frequency column is 1. This helps to highlight detections at frequencies with generally less energy. For `histonorm = 'false'` no normalisation is applied.

The wavenumber bin with the largest amplitude is picked for each frequency (=picked maxima); an error bar represents the uncertainty as the width of the corresponding peak at its half-height. The picking of maxima can be controlled by the option `SNR` (signal-to-noise ratio) set at the beginning of `plot_b3am.m`. A peak is only considered a maximum if its value exceeds `SNR` times the mean of the frequency column. Increasing `SNR` may exclude certain peaks from the maxima. The horizontal dashed line shows the minimum wavenumber as defined by the user in `b3am_param.m`, or set to `kmin = 1/(3dmax)` by default. It is related to the maximum wavelength `lmax = 1/kmin` that is determined by the limited aperture of the array. Waves with larger wavelength can potentially not be resolved by the array as the phase shift between stations might be too small. It is possible that multiple dispersion curves appear at certain frequencies (e.g., for the retrograde Rayleigh wave above 0.4 Hz, Figure 9). These multiple paths refer to multiple modes of the respective wave type. Often, the fundamental (=slowest) mode is the strongest, however, this depends on the local geology and can deviate in particular settings (Boaga et al., 2013).

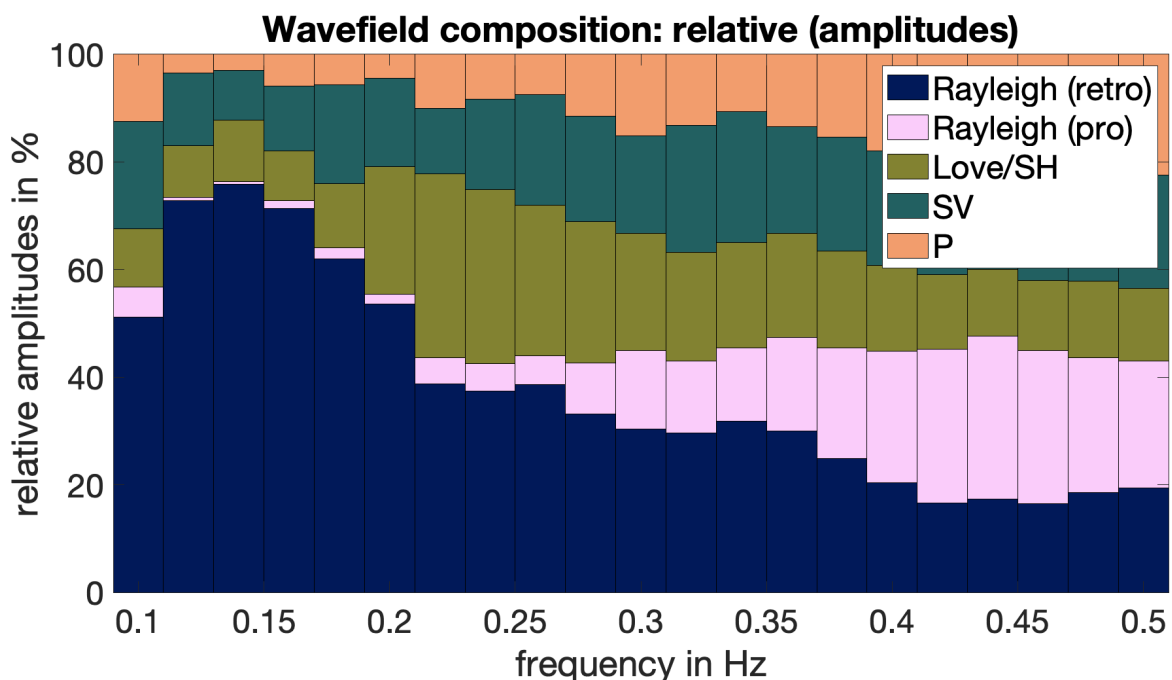


Figure 8 Bar plot of relative wavefield composition at the Parkfield array on 2 December 2002 as a function of frequency.

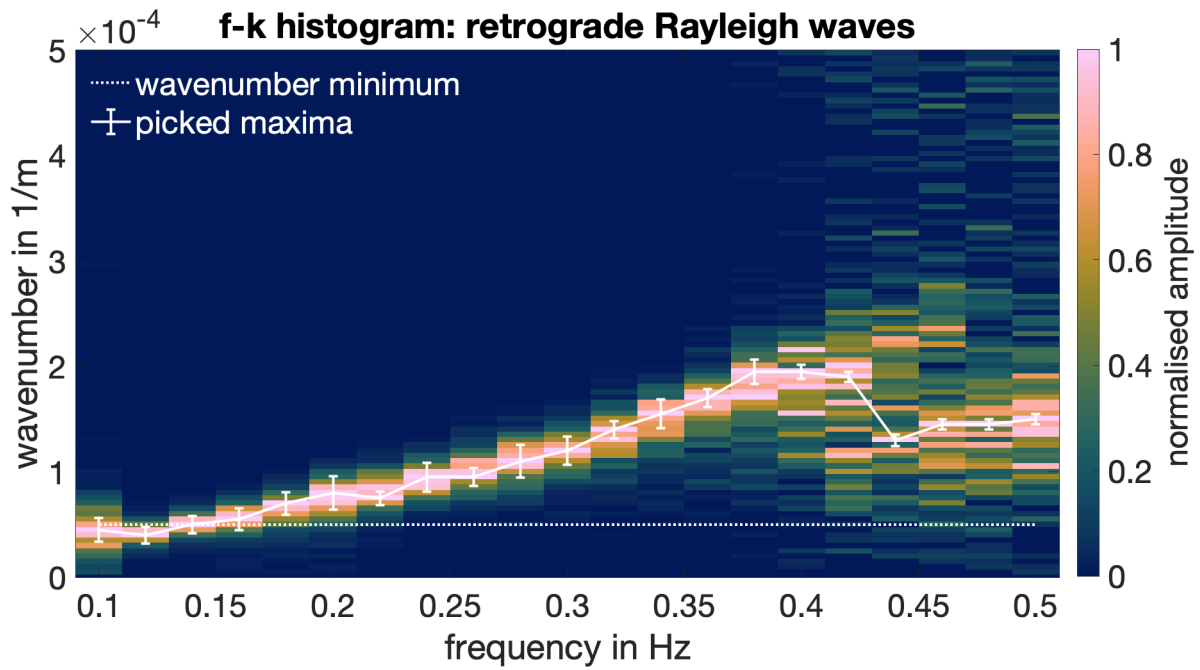


Figure 9 Normalized frequency-wavenumber (f-k) histogram of retrograde Rayleigh wave detections at Parkfield on 2 December 2002. White bars indicate the picked maxima and their errors as the width at the half height of the peak; the dotted white line denotes the given minimum wavenumber, that is, the lower confidence level for wavenumber picks.

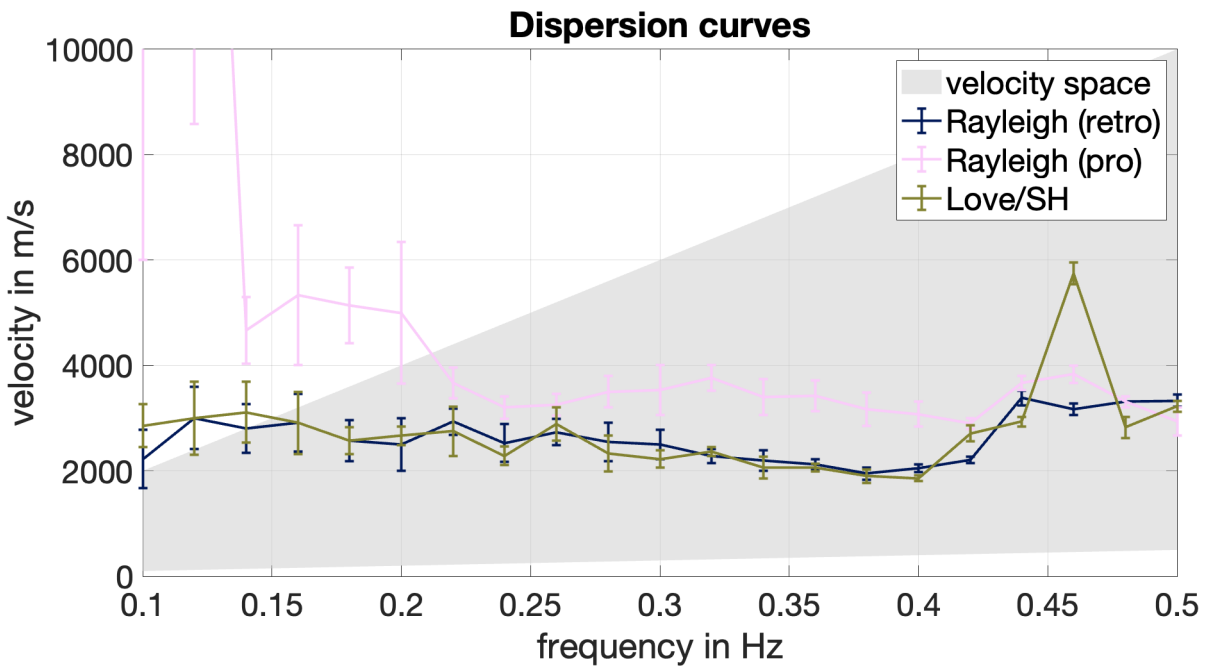


Figure 10 Dispersion curves for Love and Rayleigh waves extracted from f-k histograms (Figure 10, for example). The gray background indicates the velocity confidence zone as converted from minimum and maximum wavenumbers.

3.4.3 Dispersion curves

For the dispersion curve plot, the maxima picked in the wavenumber histograms (and corresponding uncertainties) are converted to velocities according to $v(f) = f/k(f)$ and plotted against frequency. The shaded area in the background indicates the trusted velocity space between $v_{min}(f) = f/k_{max}$ and $v_{max}(f) = f/k_{min}$. These limits relate back to the array parameters of aperture (d_{max}) and station spacing (d_{min}). If k_{min} and k_{max} are not provided, default values will be computed follow-

ing Tokimatsu’s recommendation (Tokimatsu, 1997) of $k_{max} < 1/(2d_{min})$ and $k_{min} > 1/(3d_{max})$ (cf. Equation 15). The plot of the ARF cross section (Figure 7) enables adjustment of these parameters based on the actual array design, acknowledging that station spacing and aperture may vary with azimuth (Wathelet et al., 2008). The changes made here will consequently affect the trusted velocity space plotted in the background of the dispersion curves.

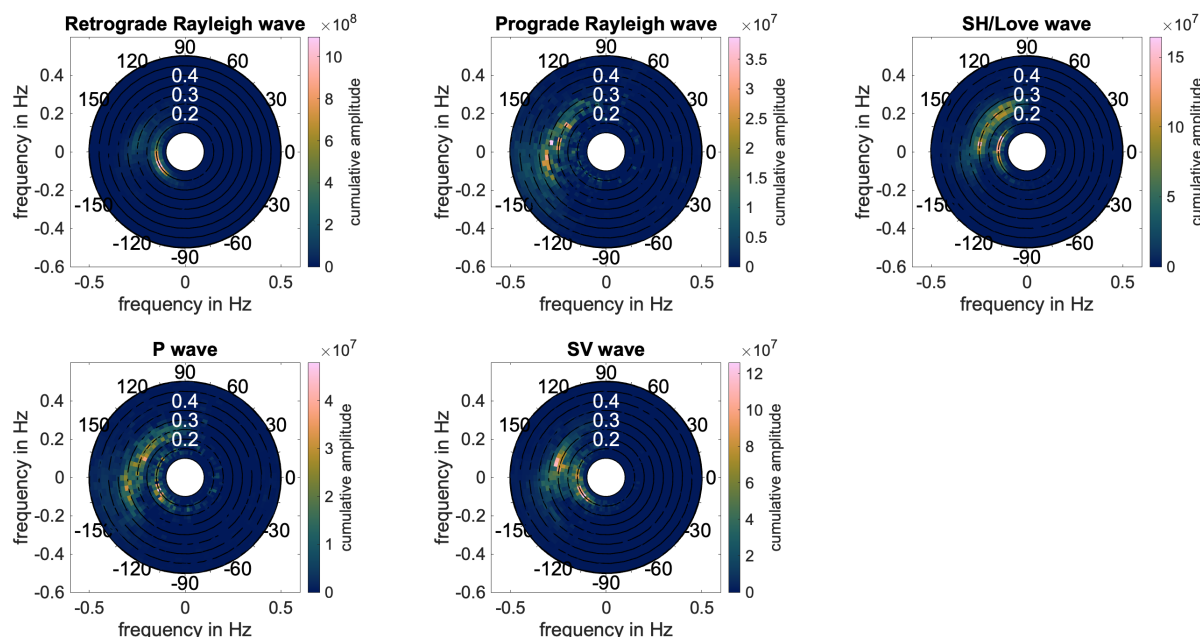


Figure 11 Polar histograms showing direction of arrival as measured for different wave types. The radial axis denotes frequency in Hz. The colourbar indicates cumulative amplitudes, that is, each detection has been weighted with the respective beam power as obtained from Equation 14.

3.4.4 Direction of arrival

In Figure 11, For each of the five polarisation types (retrograde Rayleigh, prograde Rayleigh, SH/Love, P, and SV), incoming wave energy is shown in a polar plot as a function of frequency (radial axis) and azimuth (polar axis). Detections are sorted into azimuth-frequency bins and weighted by their beam response energy; hence, the plots show not only number of detections but account for their respective amplitudes.

3.4.5 Further analysis

The output from *B3AM* provides the basis for more advanced wavefield analysis considering, for example, Rayleigh wave ellipticity (Finger and L er, 2024) or surface wave anisotropy (L er et al., 2018; Kennedy et al., 2022). All necessary information is provided with the output; its analysis and visualisation, however, requires additional scripts that correlate and plot the desired relationships (e.g., velocity as a function of azimuth in a given frequency window for anisotropy analysis). While these tools will be provided in one of the coming code updates, users are also encouraged to share the analysis tools they have developed. Further parameters to investigate could include the incidence angles of body waves as a function of propagation direction - potentially hinting at inclined subsurface reflectors - or the temporal variation of seismic velocities indicating structural changes.

4 Discussion

The *B3AM* toolbox performs frequency-wavenumber analysis on ambient seismic noise data, discriminating

different waves on account of their wave vector (propagation direction and velocity) and polarisation. It combines the analysis of multiple short time windows in histograms to produce wave type specific dispersion curves as well as azimuth-frequency plots visualising propagation velocities and direction. Further, *B3AM* provides an estimate of the wavefield composition over the analysed time period as a function of frequency, showing absolute as well as relative ratios of different surface and body wave components.

A shortcoming in the method is that SH-waves and Love waves are not automatically discriminated, as wave type identification is solely based on polarisation. SH as well as Love waves are polarised in the horizontal plane with particle motion perpendicular to the direction of propagation. While Love waves are trapped to the surface and are hence observed with their actual velocity, SH waves are body waves with a propagation path that is inclined with respect to the surface. Their apparent velocities measured at a surface array are thus much higher, so that SH waves will appear at smaller wavenumbers in the beamformer compared to Love waves. In cases where this is observed (see the Love wave f-k histogram) it might be worth filtering out the SH wave detections at low wavenumbers to improve the automatic picking of the Love wave dispersion curve.

As can be seen in the Rayleigh wave f-k histogram (Figure 9), while higher mode surface waves can show up in the histogram, they are currently not automatically discriminated in the dispersion curve analysis. Users should be aware of this and when necessary improve the automatic picks manually. We also point out here, to avoid misinterpretation, that retrograde and prograde Rayleigh waves cannot be associated one-to-

one with the fundamental and first higher mode, respectively. While indeed the fundamental (i.e., the slowest) mode Rayleigh wave often shows retrograde motion at the surface, Boué et al. (2016) show that it becomes prograde in particular settings, for example, in sedimentary basins that exhibit a large velocity contrast between the sediments and the underlying bedrock, and that a mode can change polarisation between pro- and retrograde at certain frequencies. Hence, a dispersion curve displayed for retrograde particle motion, for example, can represent a combination of different modes. We observe that the choice of temporal normalisation and time window length can affect which modes are being picked up dominantly by the beamformer, so varying these parameters can help to obtain a more complete picture.

Another important parameter in surface wave analysis is the ellipticity of Rayleigh waves (see chapter 2.2). Poggi et al. (2012) and Finger and Lör (2024), for example, use Rayleigh wave ellipticities to constrain the depth of major velocity contrasts, such as the bedrock depth under a sedimentary basin. Similar approaches use the spectral ratio between the horizontal and vertical components (HVSR; e.g., Van Ginkel et al., 2022) to infer this parameter. Equations 13a and 13b show that ellipticity can be converted into H/V ratio of Rayleigh waves, which might be more intuitive for some readers. When comparing the two, however, we need to consider that by default B3AM samples ellipticity at constant intervals between 0 and 2. Hence, for $e < 1$ the resolution of large HVSR $H/V = 1/e$ becomes quite poor. A denser sampling for values $e \ll 1$ could mitigate this effect.

Finally, while B3AM has been developed with ambient noise applications in mind, it can be (and has been) used to investigate also transient signals. Analysing the wavefield composition in a given time window provides the opportunity to discriminate different seismic phases in a transient signal where these may overlap in time and thus not be distinguishable visually/by hand. Kennedy et al. (2024), for example, used B3AM for a synthetic dataset generated with a finite-difference wavefield modelling code and successfully identified the P-wave and retrograde Rayleigh wave arrival time windows in the synthetic time series produced by a single impulsive source.

Overall, B3AM complements a new generation of ambient seismic noise methods for cheap and practical imaging and monitoring of subsurface structures and processes. Designed for three-component data analysis, B3AM fills the gap of wavefield composition analysis and wavetype specific estimates of velocity and propagation direction. Further parameters such as surface wave anisotropy or Rayleigh wave ellipticity are readily available and make B3AM an efficient toolbox for comprehensive wavefield analysis.

Acknowledgements

We thank Heather Kennedy, Ebitimi Obiri, and Lukman Inuwa for testing the code and providing feedback. Thanks to Dave Cornwell for helpful suggestions on the scope and structure of the paper, and to Ma-

rine Denolle and one anonymous reviewer for their constructive feedback that helped improve the clarity of the paper. We acknowledge Nima Riahi for providing the core scripts for three-component frequency-wavenumber analysis.

Data and code availability

All codes can be downloaded either from a GitHub repository (<https://github.com/katrinloer/B3AM>), MATLAB™ File Exchange (<https://nl.mathworks.com/matlabcentral/fileexchange/128489-b3am>), or Zenodo (<https://doi.org/10.5281/zenodo.10885984>). The example seismic data set from the Parkfield array, California, US (Thurber and Roecker, 2000), is available through the data services of the Seismological Facility for the Advancement of Geoscience (SAGE, <https://www.iris.edu>).

Competing interests

The authors have no competing interests.

References

- Aki, K. Space and time spectra of stationary stochastic waves, with special reference to microtremors. *Bulletin of the Earthquake Research Institute*, 35:415–456, 1957.
- Beyreuther, M., Barsch, R., Krischer, L., Megies, T., Behr, Y., and Wassermann, J. ObsPy: A Python toolbox for seismology. *Seismological Research Letters*, 81(3):530–533, 2010. doi: 10.1785/gssrl.81.3.530.
- Boaga, J., Cassiani, G., Strobba, C. L., and Vignoli, G. Mode misidentification in Rayleigh waves: Ellipticity as a cause and a cure. *Geophysics*, 78(4):EN17–EN28, 2013. doi: 10.1190/geo2012-0194.1.
- Boué, P., Denolle, M., Hirata, N., Nakagawa, S., and Beroza, G. C. Beyond basin resonance: characterizing wave propagation using a dense array and the ambient seismic field. *Geophysical Journal International*, 206(2):1261–1272, 2016. doi: 10.1093/gji/ggw205.
- Capon, J. High-resolution frequency-wavenumber spectrum analysis. *Proceedings of the IEEE*, 57(8):1408–1418, 1969. doi: 10.1109/PROC.1969.7278.
- Crameri, F. Scientific colour maps. *Zenodo*, 10, 2018. doi: 10.5281/zenodo.1243862.
- Curtis, A., Gerstoft, P., Sato, H., Snieder, R., and Wapenaar, K. Seismic interferometry—turning noise into signal. *The Leading Edge*, 25(9):1082–1092, 2006. doi: 10.1190/1.2349814.
- Ermert, L., Igel, J., Sager, K., Stutzmann, E., Nissen-Meyer, T., and Fichtner, A. noisi: A Python tool for ambient noise cross-correlation modeling and noise source inversion. *Solid Earth Discussions*, 2020:1–27, 2020. doi: 10.5194/se-11-1597-2020.
- Esmersoy, C., Cormier, V., Toksoz, M., and Kerr, A. Three-component array processing. *The VELA Program. A Twenty-Five Year Review of Basic Research*, 78(5):1725–1743, 1985.
- Finger, C. and Lör, K. Depth of sudden velocity changes derived from multi-mode Rayleigh waves. *Journal of Geophysical Research: Solid Earth*, 129(3):e2023JB028322, 2024. doi: 10.1029/2023JB028322.
- Gal, M., Reading, A., Ellingsen, S., Koper, K., Burlacu, R., and Gibbons, S. Deconvolution enhanced direction of arrival estimation using one- and three-component seismic arrays applied to

- ocean induced microseisms. *Geophysical Journal International*, 206(1):345–359, 04 2016. doi: 10.1093/gji/ggw150.
- Galetti, E. and Curtis, A. Generalised receiver functions and seismic interferometry. *Tectonophysics*, 532:1–26, 2012. doi: 10.1016/j.tecto.2011.12.004.
- Goldstein, P., Dodge, D., Firpo, M., and Minner, L. 85.5 - SAC2000: Signal Processing and Analysis Tools for Seismologists and Engineers. In Lee, W. H., Kanamori, H., Jennings, P. C., and Kisslinger, C., editors, *International Handbook of Earthquake and Engineering Seismology, Part B*, volume 81 of *International Geophysics*, pages 1613–1614. Academic Press, 2003. doi: 10.1016/S0074-6142(03)80284-X.
- Jiang, C. and Denolle, M. A. NoisePy: A new high-performance python tool for ambient-noise seismology. *Seismological Research Letters*, 91(3):1853–1866, 2020. doi: 10.1785/0220190364.
- Kennedy, H., Löer, K., and Gilligan, A. Constraints on fracture distribution in the Los Humeros geothermal field from beamforming of ambient seismic noise. *Solid earth*, 13(12):1843–1858, 2022. doi: 10.5194/se-13-1843-2022.
- Kennedy, H., Finger, C., Löer, K., and Gilligan, A. Surface Wave Anisotropy in Fractured Media: Insights from Wavefield Modelling and Applications for Geothermal Exploration. In *85th EAGE Annual Conference & Exhibition (including the Workshop Programme)*, volume 2024, pages 1–5. European Association of Geoscientists & Engineers, 2024. doi: 10.3997/2214-4609.2024101344.
- Lacoss, R. T., Kelly, E. J., and Toksöz, M. N. Estimation of seismic noise structure using arrays. *Geophysics*, 34(1):21–38, 1969. doi: 10.1190/1.1439995.
- Lecocq, T., Caudron, C., and Brenguier, F. MSNoise, a python package for monitoring seismic velocity changes using ambient seismic noise. *Seismological Research Letters*, 85(3):715–726, 2014. doi: 10.1785/0220130073.
- Liu, Q., Koper, K. D., Burlacu, R., Ni, S., Wang, F., Zou, C., Wei, Y., Gal, M., and Reading, A. M. Source locations of teleseismic P, SV, and SH waves observed in microseisms recorded by a large aperture seismic array in China. *Earth and Planetary Science Letters*, 449: 39–47, 2016. doi: 10.1016/j.epsl.2016.05.035.
- Löer, K., Riahi, N., and Saenger, E. H. Three-component ambient noise beamforming in the Parkfield area. *Geophysical Journal International*, 213(3):1478–1491, 2018. doi: 10.1093/gji/ggy058.
- Maranò, S., Reller, C., Loeliger, H.-A., and Fäh, D. Seismic Waves Estimation and Wavefield Decomposition: Application to Ambient Vibrations. *Geophys. J. Int.*, 191(1):175–188, Oct. 2012. doi: 10.1111/j.1365-246X.2012.05593.x.
- Minio, V., Zuccarello, L., De Angelis, S., Di Grazia, G., and Saccorotti, G. MISARA: Matlab Interface for Seismo-Acoustic aRray Analysis. *Seismological Society of America*, 94(3):1689–1702, 2023. doi: 10.1785/0220220267.
- Nicolson, H., Curtis, A., Baptie, B., and Galetti, E. Seismic interferometry and ambient noise tomography in the British Isles. *Proceedings of the Geologists' Association*, 123(1):74–86, 2012. doi: 10.1016/j.pgeola.2011.04.002.
- Obiri, E., Löer, K., and Finger, C. Wavefield composition analysis from three-component beamforming improves thickness estimates of sedimentary layers. In *84th EAGE Annual Conference & Exhibition*, volume 2023, pages 1–5. European Association of Geoscientists & Engineers, 2023. doi: 10.3997/2214-4609.2023101004.
- Poggi, V., Fäh, D., Burjanek, J., and Giardini, D. The use of Rayleigh-wave ellipticity for site-specific hazard assessment and microzonation: application to the city of Lucerne, Switzerland. *Geophysical Journal International*, 188(3):1154–1172, 2012. doi: 10.1111/j.1365-246X.2011.05305.x.
- Qin, T. and Lu, L. Improved beamforming schemes for estimation of multimode surface wave dispersion curves from seismic noise with reducing effect of the irregular array geometry and/or anisotropic source distribution. *Geophysical Journal International*, 237(1):250–270, 2024. doi: 10.1093/gji/ggae038.
- Riahi, N., Bokelmann, G., Sala, P., and Saenger, E. H. Time-lapse analysis of ambient surface wave anisotropy: A three-component array study above an underground gas storage. *Journal of Geophysical Research: Solid Earth*, 118(10): 5339–5351, 2013. doi: 10.1002/jgrb.50375.
- Rost, S. and Thomas, C. Array seismology: Methods and applications. *Reviews of geophysics*, 40(3):2–1, 2002. doi: 10.1029/2000RG000100.
- Salvermoser, J., Hadziioannou, C., and Stähler, S. C. Structural monitoring of a highway bridge using passive noise recordings from street traffic. *The Journal of the Acoustical Society of America*, 138(6):3864–3872, 2015. doi: 10.1121/1.4937765.
- Schmidt, R. Multiple emitter location and signal parameter estimation. *IEEE transactions on antennas and propagation*, 34(3): 276–280, 1986. doi: 10.1109/TAP.1986.1143830.
- Sollberger, D., Heimann, S., Bernauer, F., Eibl, E. P., Donner, S., Hadziioannou, C., Igel, H., Yuan, S., and Wassermann, J. TwistPy: An open-source Python toolbox for wavefield inertial sensing techniques. In *EGU General Assembly Conference Abstracts*, pages EGU–7563, 2023. doi: 10.5194/egusphere-egu23-7563.
- Thurber, C. and Roecker, S. Parkfield Passive Seismic Array [Data set]. *International Federation of Digital Seismograph Networks*, 2000. doi: 10.7914/SN/XN_2000.
- Tokimatsu, K. Geotechnical site characterization using surface waves. In *Earthquake Geotechnical Engineering: Proceedings of IS-Tokyo'95, The First International Conference on Earthquake Geotechnical Engineering*, Rotterdam, pages 1333–136. AA Balkema, 1997.
- Van Ginkel, J., Ruigrok, E., Stafleu, J., and Herber, R. Development of a seismic site-response zonation map for the Netherlands. *Natural Hazards and Earth System Sciences*, 22(1):41–63, Jan. 2022. doi: 10.5194/nhess-22-41-2022.
- Wagner, G. S. Resolving diversely polarized, superimposed signals in three-component seismic array data. *Geophysical research letters*, 23(14):1837–1840, 1996. doi: 10.1029/96GL01599.
- Wapenaar, K. and Fokkema, J. Green's function representations for seismic interferometry. *Geophysics*, 71(4):SI33–SI46, 2006. doi: 10.1190/1.2213955.
- Wathelet, M., Jongmans, D., Ohrnberger, M., and Bonnefoy-Claudet, S. Array performances for ambient vibrations on a shallow structure and consequences over V s inversion. *Journal of Seismology*, 12:1–19, 2008. doi: 10.1007/s10950-007-9067-x.
- Wathelet, M., Chatelain, J.-L., Cornou, C., Giulio, G. D., Guillier, B., Ohrnberger, M., and Savvaidis, A. Geopsy: A user-friendly open-source tool set for ambient vibration processing. *Seismological Research Letters*, 91(3):1878–1889, 2020. doi: 10.1785/0220190360.
- Yamaya, L., Mochizuki, K., Akuhara, T., and Nishida, K. Sedimentary structure derived from multi-mode ambient noise tomography with dense OBS network at the Japan trench. *Journal of Geophysical Research: Solid Earth*, 126(6):e2021JB021789, 2021. doi: 10.1029/2021JB021789.

The article *B3AM: A beamforming toolbox for three-component ambient seismic noise analysis* © 2024 by Katrin Löer is licensed under CC BY 4.0.